High-Frequency Seismic Events on Mars Observed by InSight

M van Driel, Savas Ceylan, John F Clinton, Domenico Giardini, Anna Horleston, Ludovic Margerin, Simon C Stähler, Maren Böse, Constantinos Charalambous, Taichi Kawamura, et al.

High frequency seismic events on Mars observed by InSight

M. van Driel[1], Savas Ceylan[1], John F. Clinton[2], Domenico Giardini[1], Anna Horleston[3], Ludovic Margerin[4], Simon C. Stähler[1], Maren Böse[2], Constantinos Charalambous[5], Taichi Kawamura[6], Amir Khan[1,7], Guenolé Orhand-Mainsant[8], John-R. Scholz[9], Fabian Euchner[2], Martin Knapmeyer[10], Nicholas Schmerr[11], William T. Pike[5], Philippe Lognonné[6,12], William B. Banerdt[13]

[1]Institute of Geophysics, ETH Zurich, Zurich, Switzerland
[2]Swiss Seismological Service, ETH Zurich, Zurich, Switzerland
[3]School of Earth Sciences, University of Bristol, Bristol, UK
[4]Institut de Recherche en Astrophysique et Planétologie, Université Toulouse III Paul Sabatier, CNRS, CNES, Toulouse, France
[5]Department of Electrical and Electronic Engineering, Imperial College London, London, UK
[6]Université de Paris, Institut de physique du globe de Paris, CNRS, Paris, France
[7]Institute of Theoretical Physics, University of Zürich, Zürich, Switzerland
[8]Institut Supérieur de l'Aéronautique et de l'Espace SUPAERO, Toulouse, France
[9]Max Planck Institute for Solar System Research, Göttingen, Germany
[10]DLR Institute of Planetary Research, Berlin, Germany
[11]Department of Geology, University of Maryland, College Park, College Park, MD, USA
[12]Institut Universitaire de France, 1 rue Descartes, Paris, France
[13]Jet Propulsion Laboratory, California Institute of Technology, Pasadena, CA, USA

Key Points:

- InSight's seismometers have recorded several hundreds of events at frequencies between 1 and 10 Hz.
- The envelopes of these events can be explained by seismic waves guided in the crust over significant distances.
- This observation helps to constrain the elastic properties of the shallow structure.

Corresponding author: Martin van Driel, `vandriel@erdw.ethz.ch`

Abstract

The seismometer deployed on the surface of Mars as part of the InSight mission (**In**terior Exploration using **S**eismic **I**nvestigations, **G**eodesy and **H**eat **T**ransport) has recorded several hundreds of marsquakes in the first 478 sols after landing. The majority of these are classified as high frequency events in the frequency range from approximately 1 to 10 Hz on Mars' surface. All the high frequency events excite a resonance around 2.4 Hz and show two distinct but broad arrivals of seismic energy that are separated by up to 450 s. Based on the frequency content and vertical-to-horizontal energy ratio, the high frequency event family has been subdivided into three event types, two of which we show to be identical and only appear separated due to the signal-to-noise ratio. We show here that the envelope shape of the HF events is explained by guided Pg and Sg phases in the martian crust using simple layered models with scattering. Furthermore, the relative travel times between these two arrivals can be related to the epicentral distance, which shows distinct clustering. The rate at which HF events are observed varies by an order of magnitude over the course of one year and cannot be explained by changes of the background noise only. The high frequency content and the absence of additional seismic phases constrain crustal attenuation and layering, and the coda shape constrains the diffusivity in the uppermost shallow layers of Mars.

Plain Language Summary

The high frequency events are the most commonly observed class of marsquakes by the InSight mission. As the frequency content and signal shape over time is different from seismic events (i.e. events that excite elastic waves travelling in the subsurface like earthquakes, impacts or explosions) observed both on Earth and the Moon, these were not immediately recognized as signals of seismic origin. This paper shows that these signals can be explained by distant shallow small quakes together with wave propagation effects in the martian crust. This interpretation opens the possibility to use these signals to probe the material properties of the crust and raises the question which physical process causes these events.

1 Introduction

Since the InSight lander (Banerdt et al., 2013) successfully deployed its extremely sensitive seismometer (Lognonné et al., 2019) together with a complete geophysical observatory on the surface of Mars, an unprecedented continuous data stream has become available that has opened new avenues to understanding the red planet. The first results include new observations of atmospheric (Banfield et al., 2020) and magnetic phenomena (Johnson et al., 2020). Seismological data from the very broad band (VBB) instrument that is part of the SEIS (Seismic Experiment for Interior Structure) package (Lognonné et al., 2019) have demonstrated that Mars is seismically active (Banerdt et al., 2020; Giardini et al., 2020), and information in the recorded marsquakes has been used to infer the shallow elastic structure of the planet (Lognonné et al., 2020), and will inform on deeper structure.

The seismic signals from Mars are notably different from those seen on Earth and the Moon. Figure 1 shows a spectrogram of vertical component seismic accelerations recorded by SEIS for the entirety of mission sol 421 (note mission sols are defined as martian days from landing, where a martian day lasts for $\sim 24\text{h}40'$). InSight SEIS data are available as a continuous data stream for the majority of the mission and are routinely examined by the Marsquake Service (MQS, Clinton et al., 2018, 2020; Ceylan et al., 2020) to detect seismic events on Mars. The spectrogram shown for Sol 421 shows typical seismic background noise sources for a martian sol, and is representative for the time period considered in this paper. The most obvious source for seismic noise is the martian atmosphere, notably wind and pressure fluctuations and their coupling to the InSight lander

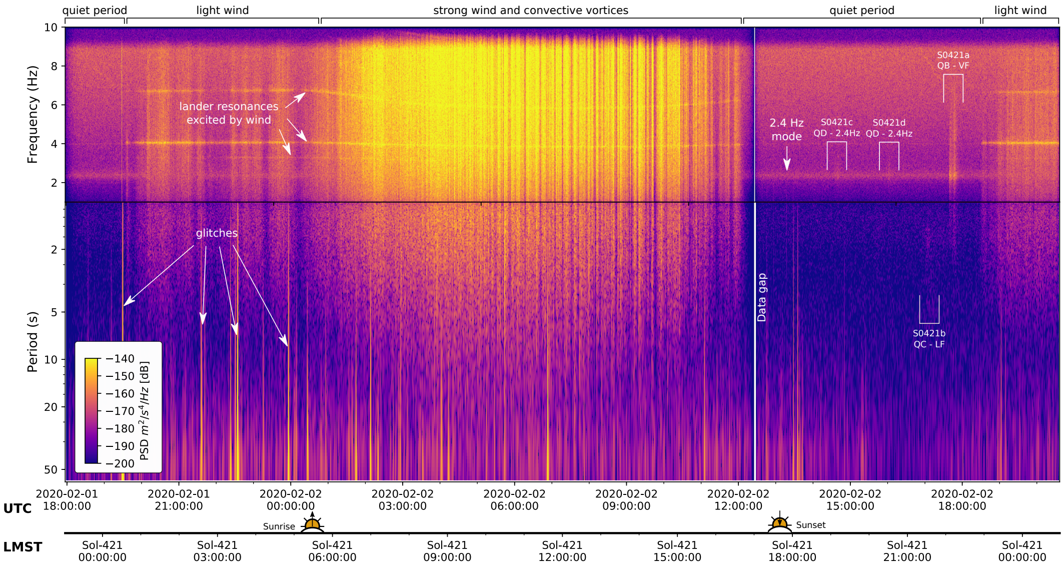

Figure 1. A representative spectrogram (PSD = power spectral density) computed for a full sol (421) of continuous vertical component VBB acceleration data sampled at 20 Hz. Annotations include the major sources of noise as well as 4 events with their unique identifier, quality and event type (discussed in text). The sunrise and sunset times are marked on the time axis (UTC is Universal Coordinated Time, and LMST is Local Mean Solar Time at the InSight landing site).

observed during the sunlit portion of the day (Ceylan et al., 2020; Lognonné et al., 2020). Sol 421 also exhibits bursts of energy visible across a broad band of frequencies, that are manifested as vertical bright-colored lines in Figure 1; these are glitches (Scholz et al., 2020; Lognonné et al., 2020, SI5), that are caused by thermally induced events within the SEIS instrument assembly resulting in a small tilt of the seismometers. Horizontal bands of energy at higher frequencies are wind-induced spacecraft resonances, and there is an intriguing resonance at around 2.4 Hz that is present at all times, even when the atmospheric background noise is low. While insensitive to wind excitation, this resonce is amplified during seismic events (Giardini et al., 2020).

Sol 421 exhibits a total of four seismic events detected by the MQS (S0421a-d) of different types that are representative of martian seismicity. Giardini et al. (2020) introduced the classification of two distinct families of martian seismic events, separated by their frequency content into high- and low-frequency events (henceforth HF and LF family, respectively). Frequency content differences are readily seen in Figure 1 where 421a, 421c, and 421d are classified as HF events, and 421b is assigned to the LF event category. The frequency content classification is also apparent in power spectra computed for individual event time windows, Figure 2 shows that while the HF family of events has energy predominantly above 1 Hz, the LF family has its main energy at frequencies below this value. Figures 1 and 2 show that there is significant variation within the HF family with respect to the spectral content and energy distribution between vertical and horizontal components. That variation has motivated the MQS team to expand the event classification scheme to assign more detailed event types. Additionally to the two event families, a new event type was found more recently, it has energy at and above ~ 8 Hz (not shown here), is attributed to thermal cracking and described in detail by Dahmen et al. (2020).

When the HF events were first observed by SEIS, the origins of the signals were a puzzle, and as events with comparable frequency content and duration are unknown

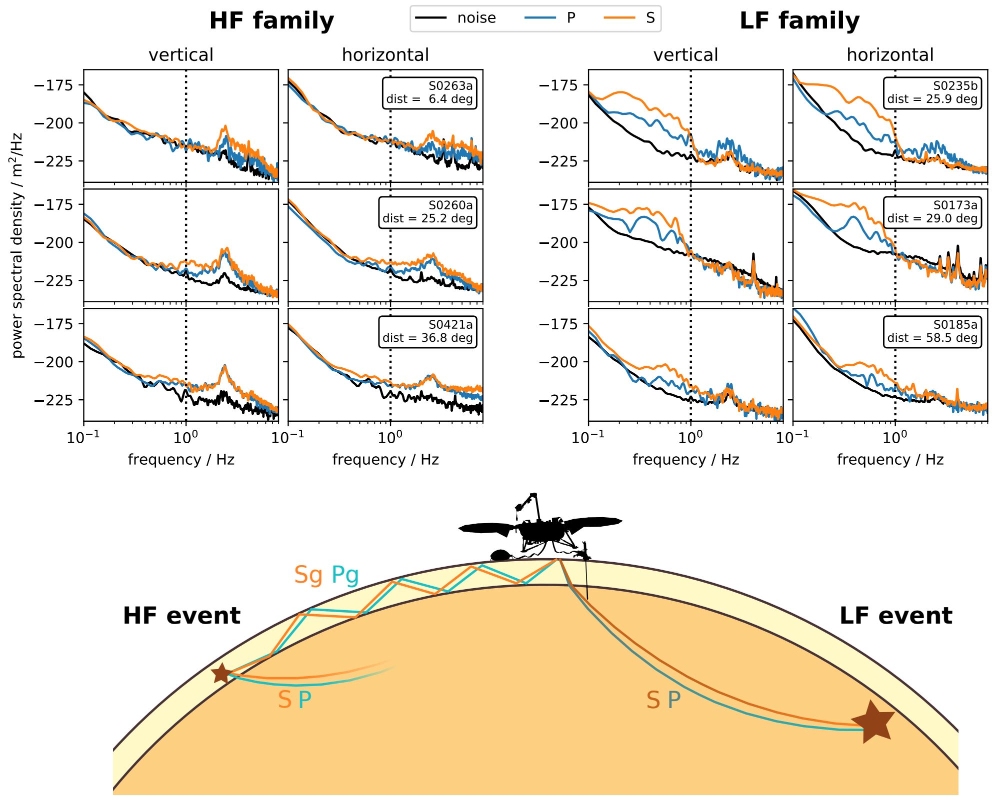

Figure 2. Top: spectra of several events from the two event families: a clear separation based on the main energy content above or below 1 Hz. Bottom: Current interpretation of the two event families: similar relative traveltime between the two main arrivals but very different frequency content can be explained by different source depth and propagation paths in the crust and upper mantle with different attenuation regimes. Figure modified from Giardini et al. (2020).

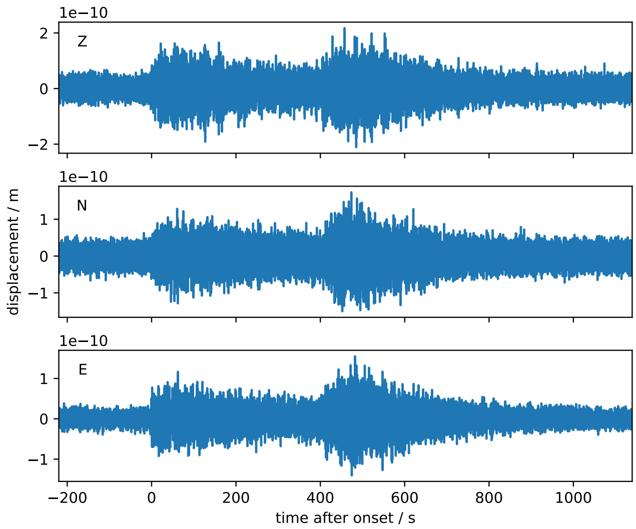

Figure 3. Three component displacement seismogram for S0421a filtered in the frequency range 0.5 – 7 Hz. The telltale sign of an HF event are the two distinct energy pulses that are separated by up to several minutes, both of which have an emergent onset and a long coda.

from terrestrial seismology, it was not clear that these are seismic signals or could potentially be generated by the lander or its interaction with the atmosphere. HF events have a characteristic bimodal rise in energy, and a a slowly decaying coda, and no distinct seismic phases (figure 3). Seismic signals from the Moon have a comparable coda duration (Latham et al., 1970), however, the envelopes do not feature two separate peaks that are typically observed with Martian HF events. Secondary arrivals within moonquakes, that are interpreted as S-waves, are typically only slope breaks within the P-wave coda, since the decay time of the P-wave train is much larger than the time separation between P and S-waves (Blanchette-Guertin et al., 2012; Lognonné et al., 2020). Another puzzle is that the majority of Martian HF events are only visible within the very narrow frequency range of the 2.4 Hz resonance, complicating the analysis. Only the largest HF event to date (S0128a) was immediately understood as being of seismic origin due to its high signal to noise ratio (SNR) and coda properties. The doublet pattern described above is now considered characteristic of the HF events and this became obvious when the number of these events increased after sol 180 in the mission. While initially the multiple arrivals were interpreted as multiple events randomly overlapping in time, it transpired then that the two arrivals correspond to a single event and that the most likely reason for the pattern are wave propagation effects. There is also considerable variation in the relative timing between the two arrivals and this was the second main reason to assume a distribution of seismic sources with varying distance, similar to the LF family (Giardini et al., 2020). In contrast, to explain this pattern with a local source requires some mechanism that excites the resonance exactly twice with several minutes time delay between the two excitations, and there is currently no obvious means for this.

To explain both the HF and LF events as being of seismic origin despite the fact that both event types have comparable relative travel times of the main arrivals, Giardini et al. (2020) argued for different propagation paths in the crust and mantle, respectively. Figure 2 shows a schematic illustration of this interpretation: the LF events are quakes that are believed to occur below the Moho and the propagation paths to the seismometer reside in the upper mantle. Attenuation then ensures the absence of high frequency signals. HF events have similar relative traveltimes between the two arrivals, so a different propagation path is needed to maintain the high frequency energy over significant distances. With a shallower source, the crust with lower attenuation and critical reflection at the Moho could act as a waveguide (Pg and Sg), while the mantle P and S waves would not be observable above the noise due to attenuation.

In this paper, we focus on the HF event family. We describe their classification and anlayse the seismic phase picks (i.e. the arrival time of the two energy pulses) as provided in the seismic catalogue (InSight Marsquake Service, 2020). Events in the HF family are divided into three subgroups based on a more detailed analysis of the spectral content of the vertical and horizontal component seismograms. We provide a detailed discussion of why these events are assumed to be crustal marsquakes and discuss the distribution of the events in terms of their distances, amplitudes, and occurrence times over the duration of the mission. Finally, we provide a wave propagation model that can explain a number of the observations, with a scattering layer in the first few kilometers over crustal models which are compatible with receiver function analysis (Lognonné et al., 2020). Based on the quantitative analysis presented here, we confirm the interpretation of the HF events as crustal quakes initially suggested by Giardini et al. (2020), and demonstrate how these signals can be used to infer subsurface properties.

2 Observations

From the beginning of the mission until March 31st 2020 (Sol 478), a total of 465 events were detected by MQS. 424 of these belong to the HF family, hence contain energy predominantly above 1 Hz and excite a local resonance of the subsurface at 2.4 Hz. As the SNR for these events is highest on the vertical component of the VBB instrument

Table 1. Event statistics until March 31st, 2020, for the three event types from the HF event family discussed in this paper. The classification is defined by Clinton et al. (2020) and is motivated by the observations discussed in section 2.1. The total number of events for each class is further detailed per event quality (A-D).

event type	abbr.	total	A	B	C	D
very high frequency	VF	23	0	9	8	6
high frequency	HF	52	0	31	18	3
2.4 Hz	24	349	0	38	137	174

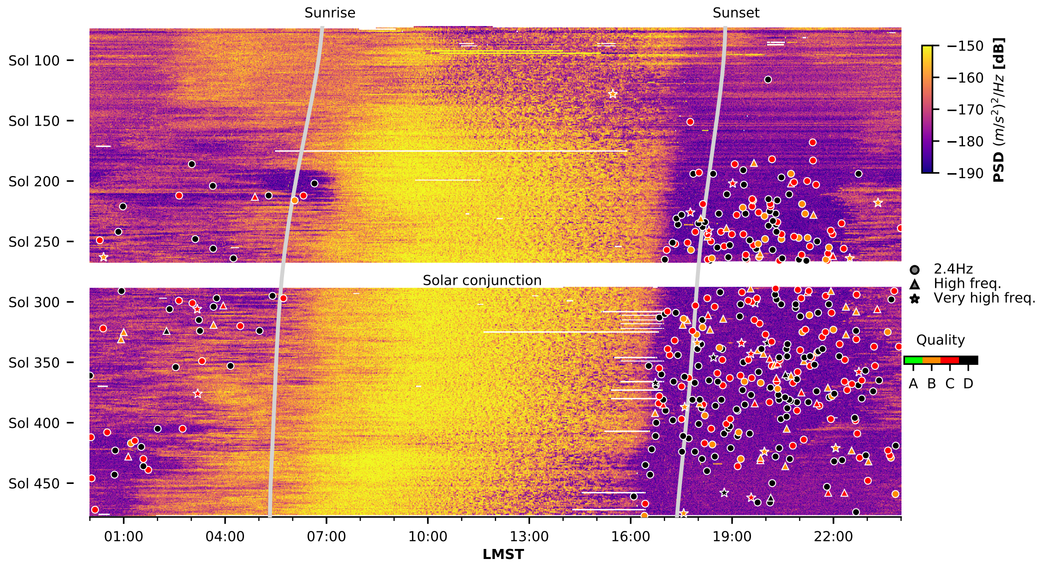

Figure 4. Evolution of the noise power spectral density (PSD) on the VBB vertical component in the 2.3-2.6 Hz frequency range (i.e. the resonance excited by events) since placement of the wind and thermal shield (WTS). For each sol, the figure shows the spectrogram as in Figure 1, but vertically constrained to the resonance as an indicator of the detection capability. The symbols indicate the distribution of the high frequency events until March 31st 2020 (sol 478) and their signal quality as detailed in the text. The noise patterns correlate with the sunrise and sunset, indicated by the white lines. Solar conjunction prohibited data transfer from sol 268 to 288.

at this resonance frequency, the MQS event detection procedures focus on this resonance and the time domain analysis in this paper is restricted to this frequency range, too.

Figure 4 shows the evolution of the noise in the frequency range of the resonance as a function of local mean solar time (LMST) and over the whole mission duration since the finalization of the instrument deployment with the placement of the wind and thermal shield (WTS, Lognonné et al., 2019). No event was observed before due to high noise levels and limited observation time during the day due to temperature constraints of the instruments. The general daily noise pattern seen in figure 1 is also visible here: while the days are very noisy due to turbulent winds (Banfield et al., 2020), the evenings and nights show windows of exceptionally low background noise. Later in the night and early morning, the wind and hence the noise increases again. This pattern is modulated by seasonal variations that lead to less favorable conditions for event detection in the beginning of the mission and most recently. The symbols that are overlain on the noise indicate occurence of the three event types from the high frequency family as detected by MQS.

In addition to event type, MQS also assigns a 'quality' to each event (ranging from A to D) to indicate how well the event can be located based on phase picking for distance and polarisation for azimuth (Böse et al., 2017). This quality is used in the analysis here to select events providing the most reliable constraints. Each event also has a unique identifier following the pattern *S[xxxx][z]*, where *[xxxx]* is a four digit number indicating the sol and *[z]* is a letter to ensure the identifier is unique in case multiple events occur on a single sol. A detailed description of MQS procedures including definitions of event types and qualities is provided by Clinton et al. (2020).

As none of the events allowed a clear determination of the back-azimuth based on polarization of the first arrival, only the distance can be estimated. For this reason, no event was classified as quality A, although a few have very high SNRs. Similar to the variation of the noise, the detection rate varies as a function of local time and mission duration. Knapmeyer and et al (2021) argue that this variability in the detection rate cannot be explained solely based on the variation of the background noise and a Poissonian random process. Table 1 summarizes the number of events of the different types and qualities used in this paper based on version 3 of the marsquake catalogue (InSight Marsquake Service, 2020) as described in detail by Clinton et al. (2020).

To facilitate the analysis of low SNR events and allow the reproducible picking of phases, we use smoothed time domain envelopes in a narrow frequency band around the resonance. The processing steps are illustrated in Figure 5 for a quality B HF event (S0260a): the broadband vertical component is first filtered to the resonance frequency range to enhance the SNR, in the second step envelopes are calculated as the absolute value of the analytical signal. Finally, the envelope is convolved with a 100 s boxcar window. An increase in the excitation of the resonance can then be detected as a change in the slope of the smoothed envelope.

Figure 6 shows the normalized envelopes of all quality B events filtered to the resonance frequency range. All of the high quality events have two clearly distinguishable arrivals, that we tentatively call Pg and Sg (Storchak et al., 2003), assuming that these arrivals are guided phases in the whole crust forming from interfering multiple reflections from the surface and the Moho. In this model, the relative time is linearly related to the distance, which we use interchangeably in the following discussion. Note that due to the relatively long averaging window, the two phases merge in the case that the time between the two phases is smaller than the window and are only visible as a break in the slope of the envelope, similar to moonquake signals recorded by Apollo (Nakamura et al., 1973).

While Figure 6a uses regular spacing on the vertical axis for the high frequency (HF) and very high frequency (VF) events (event subtypes are detailed in the next secion),

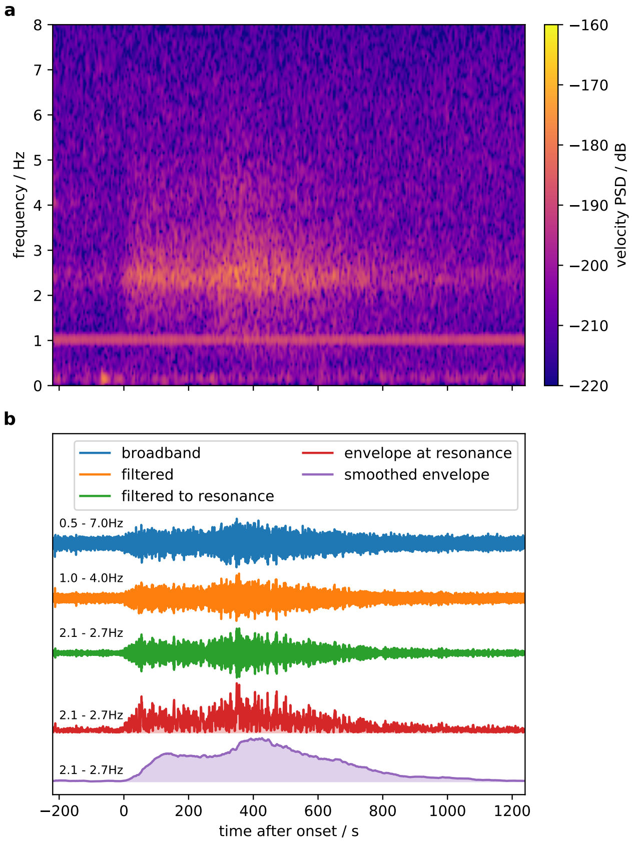

Figure 5. (a) Spectrogram of the VBB vertical component velocity for the quality B HF event S0260a. The monochromatic signal at 1 Hz is known as 'tick noise' and caused by electronic crosstalk (Ceylan et al., 2020). (b) Broad-band signal (blue, orange, green) and envelope filtered in different frequency ranges (indicated on the left above each waveform). The purple envelope has been convolved with a 100 s boxcar window. This processing maintains the onset times and thus allows picking of the two main phases also for weaker events.

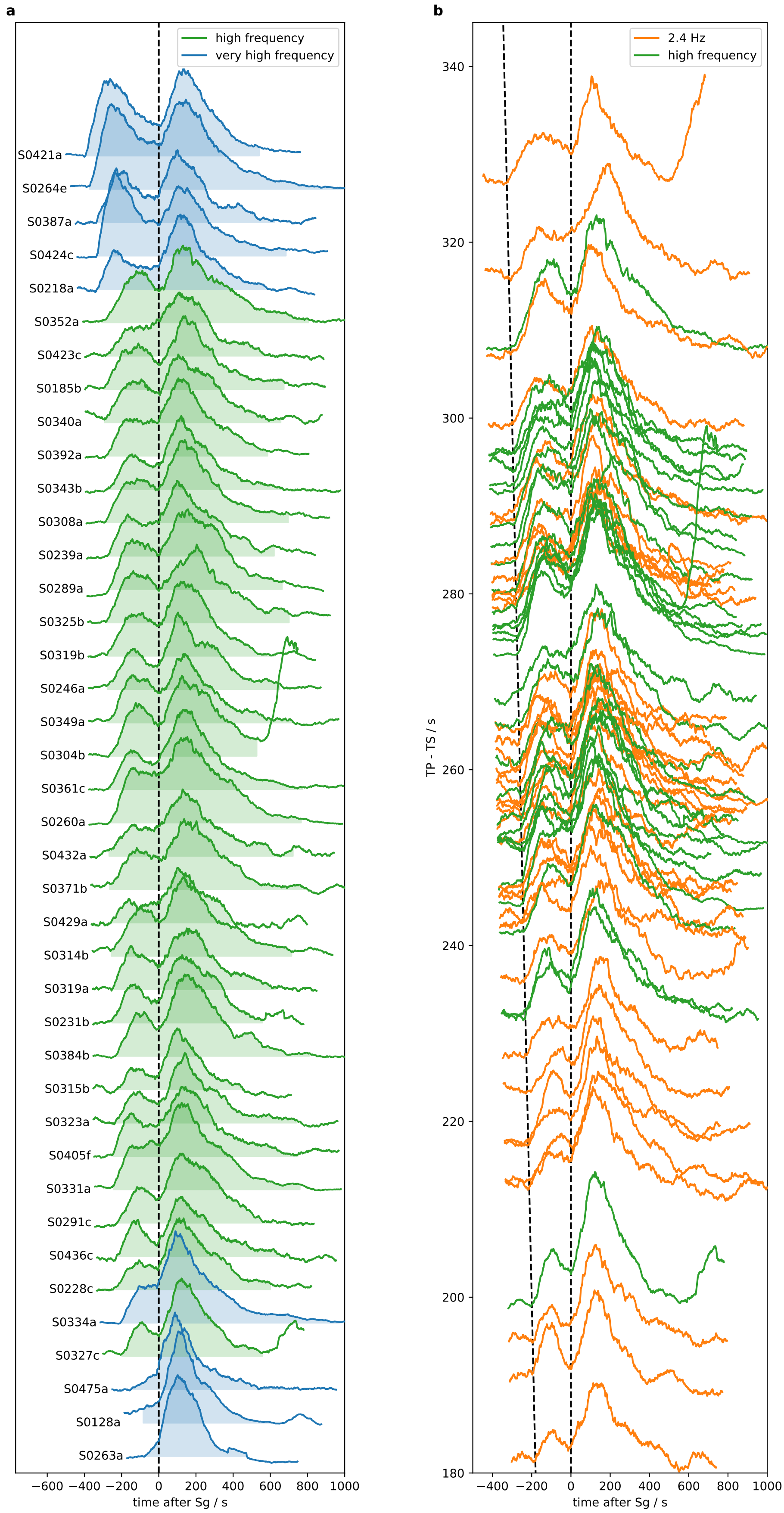
a
high frequency
very high frequency
S0421a
S0264e
S0387a
S0424c
S0218a
S0352a
S0423c
S0185b
S0340a
S0392a
S0343b
S0308a
S0239a
S0289a
S0325b
S0319b
S0246a
S0349a
S0304b
S0361c
S0260a
S0432a
S0371b
S0429a
S0314b
S0319a
S0231b
S0384b
S0315b
S0323a
S0405f
S0331a
S0291c
S0436c
S0228c
S0334a
S0327c
S0475a
S0128a
S0263a
−600 −400 −200 0 200 400 600 800 1000
time after Sg / s
b
2.4 Hz
high frequency
TP - TS / s
340
320
300
280
260
240
220
200
180
−400 −200 0 200 400 600 800 1000
time after Sg / s

Figure 6. (previous page) a) Normalized 2.4 Hz vertical component envelopes for all quality B HF and VF events with regular spacing, ordered by distance. b) Same for all quality B 2.4 and HF events with vertical alignment proportional to the relative arrival time of the two phases (Pg and Sg). Note that different SNRs cause the impression of different amplitudes and some events are followed by unrelated noise signals (e.g. S0304b and S0327c). Events are aligned on arrival time of the Sg phase, the filled range in (a) indicates the time window of the event as picked in the catalogue.

the events are aligned based on the time between Pg and Sg pick in Figure 6b. With the exception of event S0334a, the VF events appear at either end of the range of distances. On the other hand, HF and 2.4 Hz events overlap in their distance distribution and are virtually indistinguishable in their envelope shapes at the resonance frequency.

2.1 Spectra, Discrimination, and Excitation of the 2.4 Hz Resonance

Beyond the arrival times of the two main phases, the MQS catalogue also provides three time windows containing the main energy of the two phases and pre-event noise uncontaminated by glitches or wind gusts with the purpose of computing spectra as shown in Figure 7. Glitches (Lognonné et al., 2020, SI5) are generally less of a problem for the frequency range discussed in this paper in comparison to the LF event family, both because of their frequency content and the amplification of the signal by the resonance discussed in the following. We use the Welch estimator with a window length of 10 s to compute the displacement spectra after removing the 1 Hz tick noise (Ceylan et al., 2020) with a frequency domain muting. The SNR as a function of frequency is then estimated as the ratio of the signal to the noise spectra.

These spectra allow for the discrimination of the three event types: while 2.4 Hz events exclusively excite the resonance around 2.4 Hz, HF events contain energy above the SNR at frequencies > 4 Hz, but otherwise have a very similar spectral shape. In contrast, the VF events also excite the resonance, but contain significantly more energy at frequencies up to 10 Hz in particular on the horizontal components and in several cases reach beyond the Nyquist frequency of the VBB instrument. This provides confidence that a low amplitude VF event is unlikely to be falsely classified as 2.4 Hz or HF. There is no apparent systematic difference in the spectral shapes between the two phases in any of the event types. Similarly, no systematic variation of the spectral content with the relative traveltime is observed. Based on the spectral content, we assume that the 2.4 Hz events are low SNR versions of the same physical process as the HF events; yet some different mechanism is needed to explain the VF events.

The spectra are overlain by theoretical spectra as would be expected for a flat source spectrum (no source cut-off assumed at this point due to the unknown source size) modulated by a resonance modelled by a Lorentz function and the decay from attenuation estimated with a t^* operator (Nolet, 2009, section 5.2):

$$A(f) = A_0 + 10\log_{10}\left[\underbrace{\exp\left(-\pi f t^*\right)}_{\text{attenuation}}\underbrace{\left(1+\alpha\left[1+\frac{(f-f_0)^2}{(f_w/2)^2}\right]\right)^{-1}}_{\text{amplification by resonance}}\right] \tag{1}$$

Here we chose A_0 to match the normalization at the peak of the resonance, t^* varies between 0.05 s and 0.5 s, the peak frequency of the resonance is $f_0 = 2.4$ Hz and the width of the resonance is chosen empirically to $f_w = 0.3$ Hz. The amplification factor of the

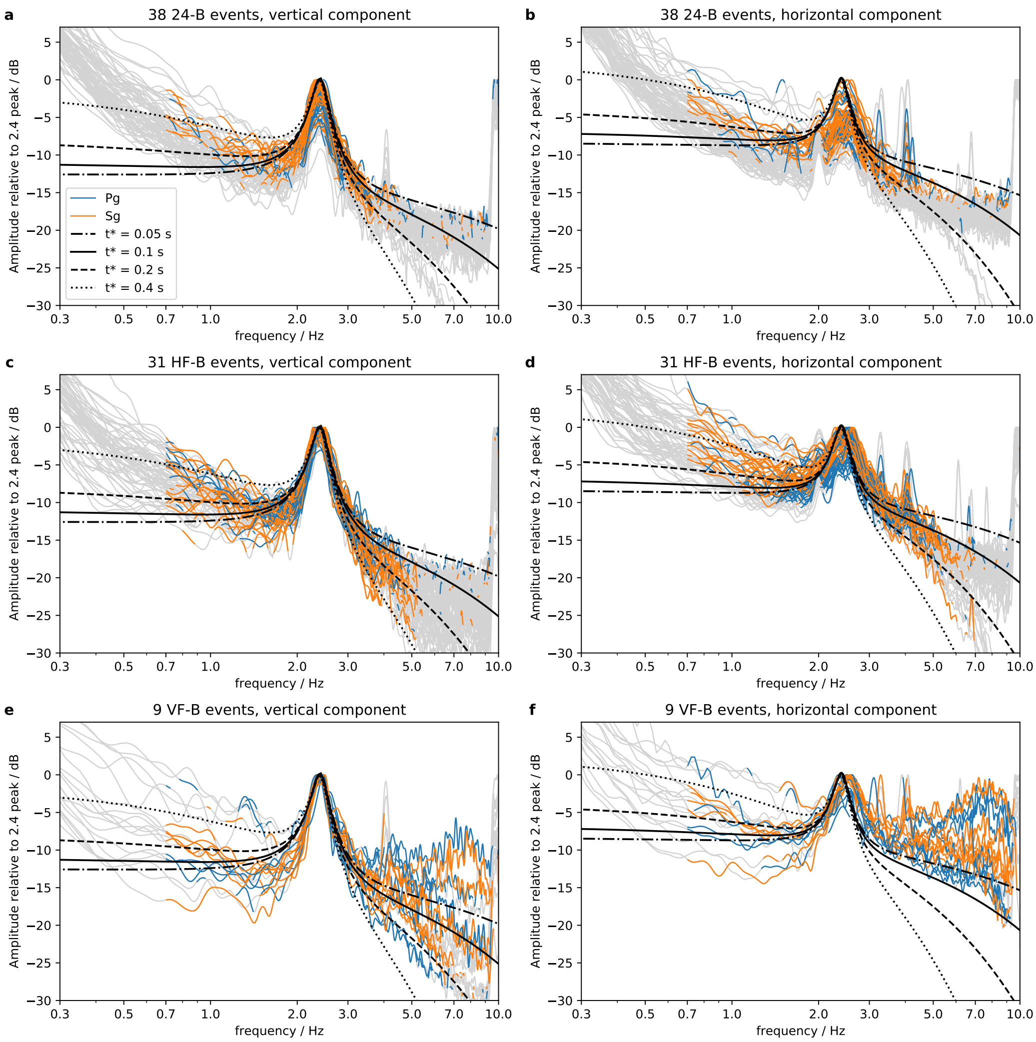

Figure 7. Displacement spectra for quality B 2.4 Hz (a-b), HF (c-d) and VF (e-f) events for vertical (a, c, e) and horizontal components (b, d, f). For frequencies above 0.7 Hz, the lines are colored where the SNR is above a value of 2. Black lines indicate expected spectra assuming a flat source spectrum modulated by a resonance (amplification factors 30 on the vertical and 10 on the horizontal) and frequency independent attenuation with different quality factors. The difference in amplitude at frequencies about 5 Hz is the main discriminant between the HF and VF event classes.

resonance is stronger on the vertical ($\alpha = 30$) than on the horizontal ($\alpha = 10$). While this model can fit the spectra of the 2.4 Hz and HF events to a high degree, this is not the case for the VF events where the spectral power even increases with frequency in several cases and differs strongly between vertical and horizontal component.

Using a t^* value of 0.2 s as upper bound and assuming a total traveltime t for the Sg window used to compute the spectra of 500 s (approximately the time between the Pg onset and the maximum energy of Sg for the largest cluster of events), a lower bound for the quality factor averaged over the ray paths that contribute to this arrival can be derived as $Q_{\text{eff}} = t/t^* > 2500$. This estimate includes both intrinsic attenuation as well as scattering and as such provides a lower bound for the quality factor for the intrinsic attenuation. This lower bound was previously proposed by Giardini et al. (2020) based on the same argument but with much fewer events and is compatible with the minimum intrinsic Q_i values proposed by Lognonné et al. (2020) based on coda scattering analysis. Importantly, our argument for a lower bound on Q_i is consistent with the assumption of a flat source spectrum; a potential deficiency of high frequencies at the source would require even higher values for Q_i.

A further observation is the systematic shift of the peak frequency of the resonance towards higher frequencies on the horizontal in comparison to the vertical component. The exact mechanism, structural interpretation, and excitation of the resonance will be discussed in a future paper. For present purpose, we just assume that the resonance amplifies seismic waves from the subsurface.

2.2 Distance Estimates and Distribution

Assuming that the two arrivals correspond to the crustal Pg and Sg arrivals and assuming crustal velocities, the relative traveltime is linearly related to distance. With this distance, the amplitudes can be converted to a magnitude. Here, we follow the same approach and use the same crustal velocities as in Giardini et al. (2020), i.e. $v_s = 2.3$ km/s and $v_p = 1.7 v_s$. For further details on the magnitude scales we refer to Böse et al. (2018); Clinton et al. (2020).

Figure 8 a) and b) show the amplitudes and corresponding magnitudes, respectively, for all pickable (i.e. quality B and C) events for the three different event types. The amplitudes are estimated as the peak amplitude of a Lorenz curve fit to the displacement spectra between 2 and 3 Hz (Giardini et al., 2020, SI3). As the noise in the evening was very consistent over large parts of the mission, there is also a clear detection threshold of about −219 dB for the 2.4 Hz and HF events, while this value seems to be higher for the VF events at distances larger than about 20°. The dashed line at −212.5 dB indicates an approximate separation between the 2.4 Hz and HF events. This is consistent with these events having the same spectral properties, but the HF being larger so that they reach above the noise also outside the resonance. In other words, the resonance improves the signal to noise ratio by about 6.5 dB, as it amplifies the seismic signals stronger than the background noise; a large fraction of the events in the catalogue (i.e. the 2.4 Hz events) are only observable due to this amplification.

The distance clustering of the HF and 2.4 Hz events discussed above is also apparent here and we use Gaussian kernel density estimation (KDE) in figure 8 c) to approximate the distance distribution. To verify if the distance clustering can be explained by a homogeneous distribution of quakes and the geometric increase of surface area with approximately the square of distance combined with a distance dependent detection threshold, we also compute the KDE with a weighting of each event with its distance squared. As the shape of the weighted KDE maintains the clear peak and sharp cutoff at around 30 degrees, we conclude that the 2.4 Hz and HF events are in fact clustered in distance. On the other hand, for the VF events the weighted KDE is monotonically decreasing (besides the very close range where the number of events is too small to do statistics), which

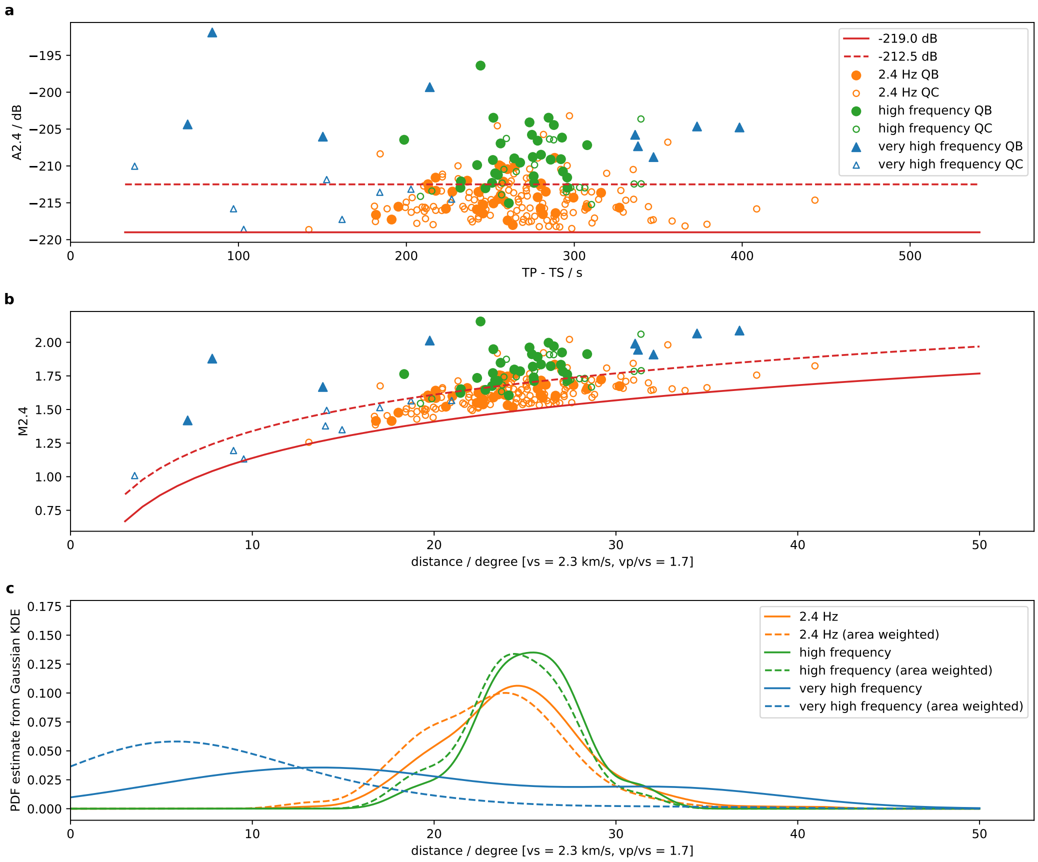

Figure 8. (a) Spectral amplitude measured on the 2.4 Hz resonance Vs. relative arrival times of Pg and Sg. The red solid line represents the detection thresholds during the quietest times of the mission and the red dashed line indicates the amplitude at which most events are visible outside the resonance. (b) Assuming seismic velocities, distances in degrees and Magnitudes can be assigned. (c) Kernel density estimation with distances weighted according to the corresponding surface area confirms that 2.4 Hz and HF events are clustered around a relative traveltime of 280 s, while VF events are more evenly distributed.

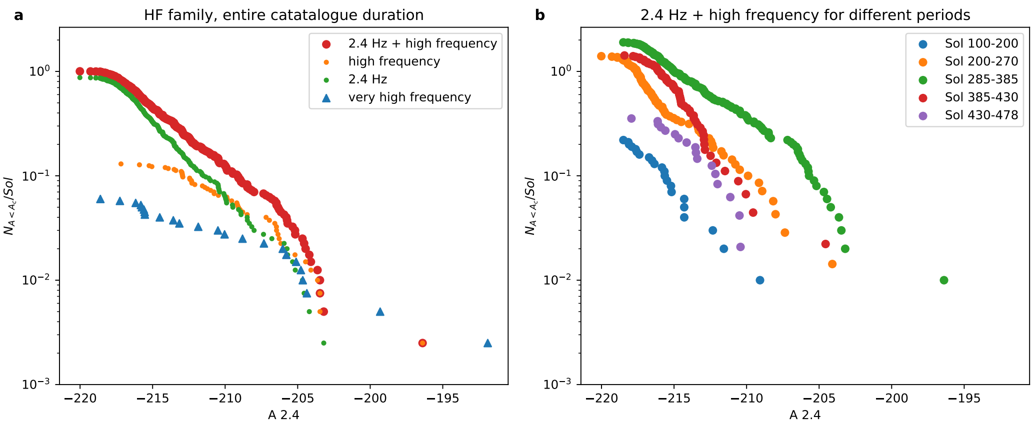

Figure 9. a) Cumulative size-frequency distribution normalized to one sol for the different event types. b) Same for 2.4 Hz and HF events combined for several time windows in the mission. The number of events per sol varies by more than an order of magnitude, which is significantly more than the variation in the noise level and length of the quiet evening windows.

is consistent with a homogeneous distribution over the surface and a distance-dependent detection threshold.

2.3 Size-frequency distribution

The size-frequency distribution of events is commonly used to understand the rate and relative distribution of large versus small events, as well as providing an indication of catalogue completeness and maximum size of the events. To avoid using a propagation model and to plot the raw data, we use the amplitude on the resonance as the size measure and then plot the cumulative distribution of the different event types in Figure 9 a). Again the 2.4 Hz events appear as smaller versions of the HF events in that the completeness of the catalogue is at approximately 6.5 dB lower than for the HF events. When plotting both event types combined, the events show a linear trend in the logarithmic scale until reaching a more rapid roll off at a maximum amplitude of about −203 dB. The single outlier corresponds to event S0331a, which is the only event that was strong enough to be observed during the more noisy periods of the day and hence can be expected to follow a different statistic.

The VF events follow a significantly shallower slope in the size-frequency distribution, meaning that that the fraction of high amplitude events is much higher. For the VF events the two largest events appear less as outliers but may be more easily explained by linear extrapolation from the smaller events. A maximum size is hence less apparent for the VF events than for the other event types. Curiously, the largest event with a significant margin in the VF class was also the first to be observed (S0128a), which may of course be a coincidence.

2.4 Temporal Evolution

As is obvious from Figure 4, the event rate varies greatly over time, with almost no event in the first 100 sols and several events per sol around the conjunction. The question if this variation can be explained just by variation of the background noise and a Poissonian random process is addressed in detail by Knapmeyer and et al (2021), with the conclusion that the event rate in fact varies. Knapmeyer and et al (2021) also com-

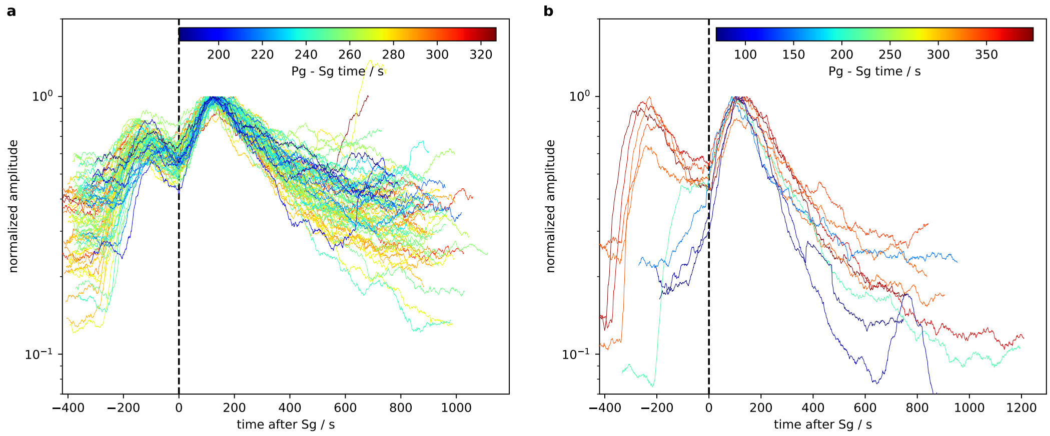

Figure 10. All quality B 2.4 Hz and HF events (a) ase well as VF events (b) aligned on the Sg arrival and scaled to the same amplitude. The color of each line corresponds to the relative traveltime, note the different colorbars. The coda shape of the Sg phase has no significant systematic dependency on the distance for 2.4 Hz and HF events in contrast to the VF events.

pare the event rates to several hypothesized sources of such a seasonality, such as seasonal cooling, atmospheric pressure variations and solar tidal strain rates.

In Figure 9 b) we plot the cumulative size-frequency distribution for 2.4 Hz and HF events combined for five different time windows of the mission. We confirm that the difference in total event rates can not be explained by a variation of the completeness, that is the smallest events that can be observed due to the noise and consequently the number of small events. In contrast, also the higher amplitude events that would have been seen in all phases of the mission show reduced rates in the beginning and most recent time windows.

Furthermore, the slope of the distribution remains unchanged, which may be used as a hint that the source mechanism remains the same. The same argument can be applied to the unchanged distance distribution (not shown here).

2.5 Envelope Shape

Finally, we observe that the shape of the Sg envelope and coda decay appears not to depend systematically on distance for the 2.4 Hz and HF events in time windows where the signal has good SNR. In contrast, there may be such an effect for the VF events (Figure 10). We cannot exclude the possibility though that we do not observe this for the 2.4 Hz and HF events, as these events cover a smaller distance range and even the highest quality events have a lower SNR than the VF events. For the VF events, there is a trend to a faster coda decay for closer events, as well as a potential for the decay decreasing over time for some of the events. The apparent variability in the coda decay for the HF event is likely to be attributed in large parts to the SNR, although scattering properties of the crust could potentially vary with azimuth. However, without a better constraint on event azimuth, this remains a speculation.

As a consequence of the long coda, there is also only a weak correlation between the duration of the events and the distance, in the distance range where we have events, and duration is not a good proxy for distance estimates. Therefore, magnitude estimates for quality D events have large uncertainties.

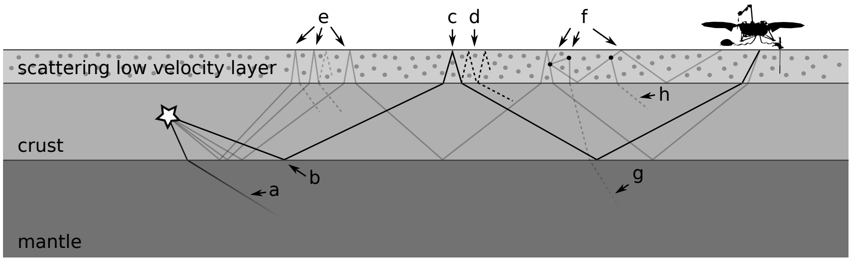

Figure 11. Ray paths that contribute to the two broad arrivals in the numerical model. Specific effects indicated by arrows are detailed in the text.

3 Interpretation

To demonstrate that the events in the high frequency family can indeed be interpreted as marsquakes, we use numerical 2D elastic wave propagation in relatively simple subsurface models to reproduce the observed envelope shapes.

3.1 Qualitative Description

As also argued by Giardini et al. (2020), the quality factor estimated based on the spectral content of the low frequency family of events is very different from the observation for the high frequency family discussed here. As a consequence, the rays have to take different paths. The high frequency signals cannot travel through the mantle where they get attenuated within a short distance. Still, the observed relative travel time of several hundreds of seconds requires distances of hundreds if not beyond 1000 km to interpret the two arrivals as P and S waves. The only way to achieve this is to have a low attenuation layer above the mantle, that guides the energy from the source to the receiver, and we tentatively interpret this layer as the crust. For the guided waves to be excited, the source needs to be inside this layer (to have post-critical reflection on the top-side of the Moho), and the sources of the low frequency events consequently have to be below.

However, the particular envelope shape observed in the data is the result of a number of effects playing together as sketched in Figure 11:

a The high frequency signals get attenuated quickly in the mantle and the low frequency part of the signal that takes a mantle path is below the noise level, when assuming a flat source spectrum.

b A velocity increase such as at the bottom of the crust reflects shallow rays with reflection coefficients close to 1.

c A low velocity layer at the surface increases the incidence angle and consequently the P-to-P reflection coefficient. This is critical, as P-to-S converted phases have a higher incidence angle at the bottom of the crust than both the S and the P phase (e.g. Kennett, 1989) and are more likely to pass into the mantle, where the energy would be lost to attenuation. This would prevent the Pg phase from developing.

d Reverberations in the shallow layer distribute the energy over time on each surface reflection.

e The Pg and Sg phases are superpositions of PmP and SmS multiples, that is phases that get reflected at the bottom of the crust and the surface multiple times, but the number of reflections varies up to a maximum that is defined by the critical reflection at the Moho.

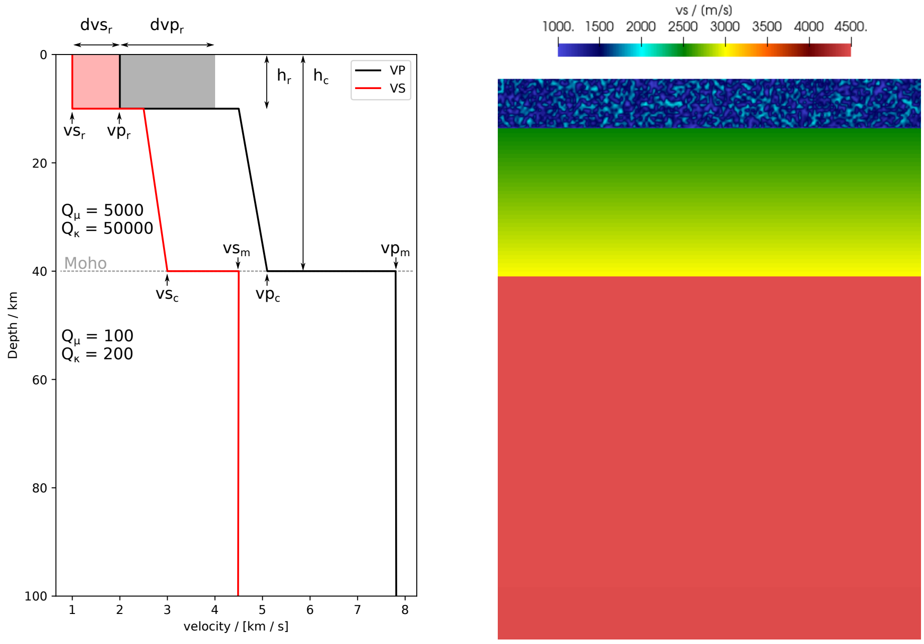

Figure 12. left: Reference model and parametrization from which all other models are created by perturbing single parameters. right: section of one random realization of the reference model.

f The shallow subsurface on Mars is assumed to be very heterogeneous. Energy that gets scattered in the shallow layer can then arrive at the receiver as a more diffusive wave through the scattering layer and form the coda (compare main text and supplementary material S3 in Lognonné et al., 2020), or

g be lost to the mantle if the incidence angle is steep or

h contribute again to the Pg and Sg phases.

3.2 Numerical Model

To verify the arguments from the previous section, we run numerical elastic wave propagation simulations using the spectral element method (SEM, Afanasiev et al., 2019). 3D simulations in the parameter regime discussed here are prohibitively expensive: frequency up to 10 Hz and source receiver distances beyond 1000 km lead to a domain size of several thousands of wavelengths. For this reason we resort to 2D simulations, which are sufficient to correctly model the wave propagation phenomena sought here; yet care needs to be taken when quantitatively interpreting scattering in the shallow layer.

Figure 12 shows the reference model we use in the simulations with the 1D profile and a random realization of the scattering part. From this model, we create a series of models by perturbing individual parameters to understand the sensitivity of the signal shape to the particular subsurface structure. The parameters are indicated in the figure as crustal thickness (h$_c$), thickness of the shallow layer (h$_r$), crustal and mantle P and S wave velocities (Vp$_c$, Vs$_c$, Vp$_m$, Vs$_m$), minimum velocities in the shallow layer (Vp$_r$, Vs$_r$) and the range of random variation in that layer (dVp$_r$, dVs$_r$). The random velocities in the scattering medium are independently and equally distributed on each point of the model grid which has a spacing of one S wavelength at a frequency of 2 Hz, corresponding to 500 m in the reference model. In between the gridpoints the model is linearly interpolated to the numerical SEM mesh. The vertical extent of the domain is 200 km so that mantle ray paths are in principle also possible, but these experience the

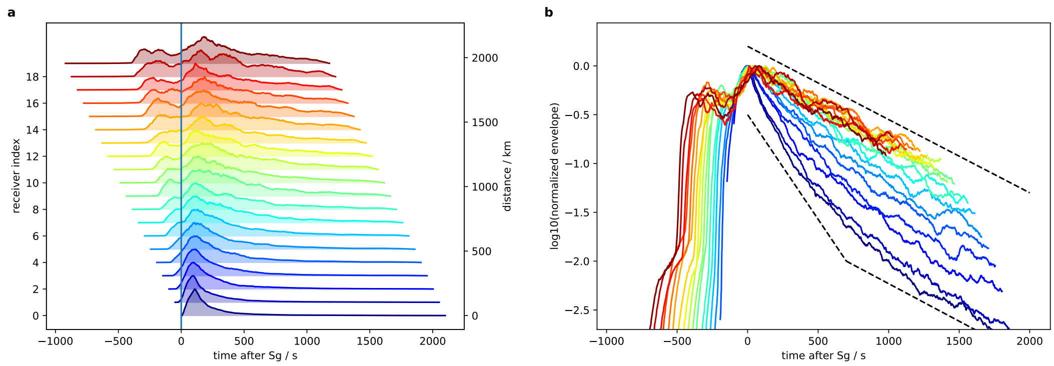

Figure 13. Envelopes of synthetic seismograms computed in the reference model with a source at 30km depth, smoothed with a 100s boxcar window and aligned on the Sg-arrival time. The color indicates epicentral distance. The logarithmic scaling in b highlights that at later times the coda-decay is independent of the distance. For closer events, the initial decay is faster though before it approaches the same value after several hundreds of seconds as indicated by the dashed lines. The mantle P-wave is also visible as a precursor at very small amplitude.

higher attenuation in the mantle. The surface of the domain is stress-free, the other three boundaries are absorbing. Note that the range of random velocities considered here refers to an effective 2D medium that is empirically built to resemble the observed coda properties and should be interpreted with care as the scattering is inherently a 3D effect.

The source is a normal fault with the fault plane inclined by 45° at 30 km depth. However, tests with a variation of the source (not shown here) reveal a low sensitivity of the envelope shapes with respect to the particular source mechanism. 20 receivers are regularly spaced starting from the source location and placed on the surface. To get comparable relative travel times and envelope shapes across the models, the receiver distance is adapted for each model based on the approximation that the Pg and Sg times are predicted by the velocities at the bottom of the crust. The furthest receiver is chosen to have an approximate relative traveltime of 300 s and hence a distance of:

$$\Delta_{300} = \mathrm{Vp}_c \mathrm{Vs}_c / (\mathrm{Vp}_c - \mathrm{Vs}_c) \cdot 300\,\mathrm{s} \tag{2}$$

For the reference model, the maximum receiver distance is therefore $\Delta_{300} = 2186\,\mathrm{km}$

After high-pass filtering at 0.5 Hz, we compute synthetic envelopes in the same way as for the data in section 2. The results in figure 13a show significant similarities to the data in figure 6: the two energy packages corresponding to guided Pg and Sg phases can be produced by wave-propagation effects in this simple model. The general pattern of an increasing Pg to Sg amplitude with distance can also be reproduced as well as the appearance of random amplitude modulations that are not consistent across multiple stations/distances.

Furthermore, Figure 13b shows that the Sg coda shows exponential decay on two different time scales, where the longer time scale is dominating for the distance where the HF events are clustered. For closer events, an initial steeper decay in the first few hundreds of seconds can be observed, as indicated by the dashed lines. We attribute these different decay times to the leakage of energy from the shallow layer and the whole crust,

Table 2. Parameter range explored in the sensitivity analysis.

parameter	abbr.	Figure 14	reference value	range
crustal thickness	h_c	a	40 km	30-60 km
crustal velocities	Vs_c	b	3.0 km/s	2.1-3.9 km/s
	Vp_c	b	5.1 km/s	3.6-6.6 km/s
scattering layer thickness	h_r	c	10 km	5-20 km
scattering layer velocities	Vs_r	d	1.0 km/s	0.5-2.0 km/s
	Vp_r	d	2.0 km/s	1.0-4.0 km/s
scattering strength	dv_r	e	100%	50%, 10%
crustal layering/gradient		f		
mantle velocities	Vs_m		4.5 km/s	
	Vp_m		7.8 km/s	

respectively. As discussed in section 2.5, there may be a hint of such difference in the coda decay as a function of distance for the VF events in the data.

Our numerical modeling of the longer time scale exponential decay replicates the scattering behavior found in experiments designed to explain the lunar seismic coda by (Dainty & Toksöz, 1981), where a strong scattering layer with a high intrinsic Q reproduces the observed codas. From the experimental work, a similar connection was made with the signal envelopes for Apollo data, although the scattering layer likely extends to greater depth on the Moon, and represents the division between fractured and competent rock.

As on the Moon, no evidence for surface waves is present in our data or synthetics, consistent with strong near-surface scattering. Finally, the logarithmic scaling also reveals the direct P-wave (travelling below the crust in the upper mantle) at a factor 100 below the maximum amplitude of the event, which would be invisible behind the noise in the real data.

3.3 Sensitivity Analysis

While a single simulation as shown in the previous section suffices to demonstrate that the observed signals are compatible with a seismic origin, the more difficult question is how the observations can be used to constrain the subsurface structure. To this end, we perform a sensitivity analysis to understand how each of the model parameters influences the envelope shapes. The results are shown in Figure 14 for varying each parameter as in table 2:

a - crustal thickness The main effect of changing the crustal thickness h_c from 40 km to 30 km and 60 km, respectively, while keeping the scattering layer the same, is to increase or decrease the average number of reflections at the surface and Moho on the ray path and hence the fraction of distance that the rays spend in the scattering layer. As a consequence, the arrivals are slightly later for the thinner crust and the width in particular of the Sg arrival is increased. For close-by stations, the effect on the envelope shapes is very small, confirming that these are mostly sensitive to the shallow layer.

b - crustal velocities The duration of the guided phases (without scattering) is determined by the angle of critical reflection at the Moho. Decreasing the crustal velocities Vs_c and Vp_c from 3.0 km/s and 5.1 km/s at the bottom of the crust to 2.1 km/s and 3.6 km/s thus increases the duration of both arrivals, in particular at larger distances. In contrast, increasing the velocities to 3.9 km/s and 6.6 km/s

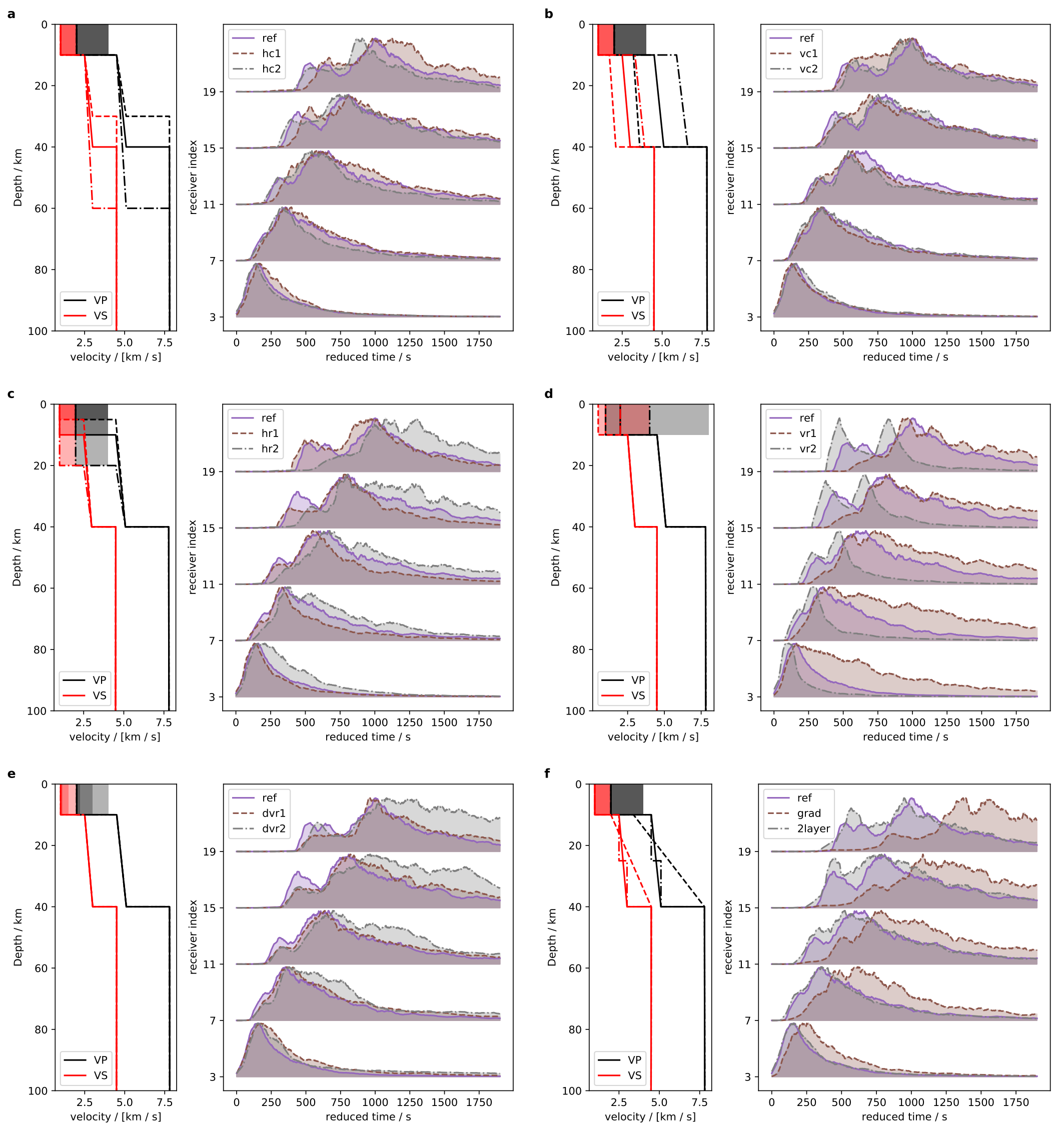

Figure 14. Sensitivity analysis for synthetic envelopes to changes in a) crustal thickness and b) velocities, c) shallow layer thickness, d) velocities and e) scattering strength. f) shows a model without a first order discontinuity at the moho and one with two crustal layers. Receivers are placed such that the estimated guided phase traveltimes based on the fastest crustal velocities are similar and hence the envelopes more directly comparable in time.

for Vs_c and Vp_c respectively, leads to shorter pulse duration in the envelope. This effect is hidden behind the additional diffusion from the scattering in the simulations.

c - scattering layer thickness The effect of variation of the scattering layer thickness h_r from 10 km to 5 km to 20 km and is very similar to variation in crustal thickness, but with opposite sign. A decrease in h_r increases the average number of reflections, while an increase in h_r reduces the reflections in the crust.

d - scattering layer velocity Here we vary the background velocities in the shallow layer Vs_r and Vp_r from 1.0 km/s and 2.0 km/s by decreasing to 0.5 km/s and 1.0 km/s and increasing to 2.0 km/s and 4.0 km/s, while keeping the relative magnitude of the velocity variations constant. This parameter controls the time spent in the shallow layer, but more importantly also the chance for scattered energy to be trapped in the shallow layer and hence contributes to multiple scattering. This parameter has a strong effect on the partitioning of the energy between the ballistic arrivals and the coda; higher velocities lead to much clearer peaks. Furthermore, the exponential decay rate of the coda strongly depends on this parameter, where more scattering leads to slower diffusion of the energy. This is the strongest effect on close by events. Additionally, this parameter also controls the P-to-P reflection coefficient at the surface by changing the incidence angle and in this way determines the Pg/Sg amplitude ratio. However, this effect is masked here by the scattering and not visible in the simulation.

e - scattering strength Reducing the scattering from a maximum velocity contrast of 100% to 50% and 10% for models dvr1 and dvr2 respectively demonstrates that with lower scattering, the end of the Sg phase is more sudden, as the SmS multiples approach the critical reflection angle. Exponential coda decay is then only observed much later than in the reference model.

f - crustal velocity gradient and layering Removing the first order velocity discontinuity of the Moho reveals that the reflection is not necessary for the guided phases to exist in principal, but bending of the rays back to the surface would be sufficient. However, the onset of the phases is significantly less impulsive due to the variation of the horizontal velocity as a function of the penetration depth of the rays. An additional layer in the crust would lead to a split of both Pg and Sg into the part that is critically reflected at the first discontinuity and the part that can still reach the Moho. This can be confirmed in the simulation as the precursor to the Pg arrival, that leads to a slope change of the envelope that cannot be observed in the data.

To summarize, while each of the parameters has a significant influence on the envelope shapes, trade-offs between them make it difficult to determine a single set of preferred parameters. The reference model is therfore just an example of a model that produces signals similar to the data and as such proves the possibility of a seismic interpretation, but the range of possible models remains large without additional constraints. Furthermore, for distance estimation as required in the marsquake catalogue (Clinton et al., 2020), a linear move-out assumption for the onset of the phases using the velocity in the lower crust appears as an appropriate approximation. The velocity currently used by MQS ($v_s = 2.3\,\mathrm{km/s}$, $v_p/v_s = 1.7$) falls well in the range of models tested here (in particular fig. 14b). However, both faster and slower velocities may be appropriate with consequences for distance and magnitude estimates. Furthermore, the shallow layer suggested by Lognonné et al. (2020) based on receiver functions ($8-11\,\mathrm{km}, v_s = 1.7-2.1\,\mathrm{km/s}$) is close to our reference model in terms of thickness and mean S wave velocity ($10\,\mathrm{km}, v_s = 1.5\,\mathrm{km/s}$).

Our treatment of a scattering layer overlying a more transmissible layer is consistent with models of the Moon, where lunar scattering extends to a depth where pore closure and annealing of fractures removes the influence of impacts (Dainty & Toksöz, 1981).

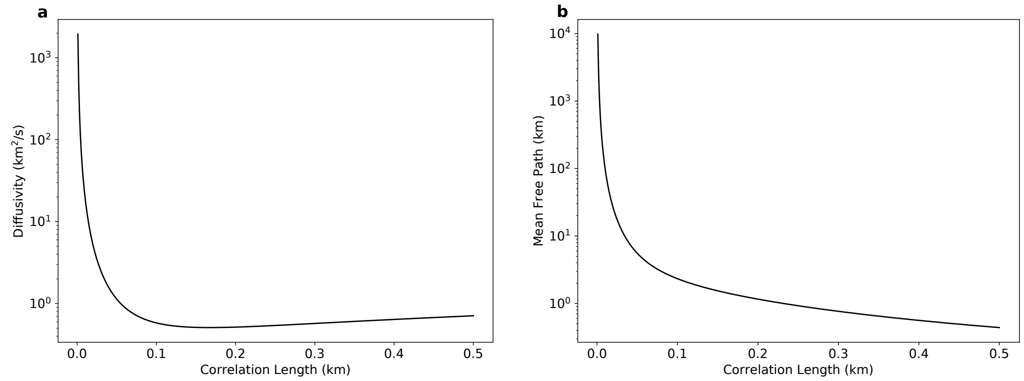

Figure 15. Estimate of the diffusivity a) and the shear mean free path b) for the heterogeneous models used in the numerical simulations, as a function of the correlation length.

Pore closure on the Moon is inferred from gravity measurements to occur with an e-folding depth of ≈ 3-30 km (Besserer et al., 2014), consistent with models of viscous pore closure due to thermal annealing (Wieczorek et al., 2013). The depth extent of cracks estimated from laboratory compaction studies of fractured basalt (Birch, 1961; Siegfried et al., 1981) suggests fracture removal takes place at pressures of ≈ 1-5 kbar (≈ 9-45 km depth in Mars). For Mars, modeling of higher crustal heat fluxes and the effects of fluids and cementation at depth shows that these processes would decrease the pore closure depth (Gyalay et al., 2020) and by inference, also reduce fracture depth, both of which are consistent with the ≈ 10 km scattering layer thickness found here.

3.4 Diffusivity Estimates

In planetary seismology, it is customary to quantify the level of heterogeneity with a parameter termed diffusivity (D, with units of km^2/s), which measures the efficacy of seismic energy transport through the medium. Indeed, when observed over sufficiently long time scales, the behavior of linear waves of any type becomes diffusive in a heterogeneous medium (Ryzhik et al., 1996; Akkermans & Montambaux, 2007). Adapting the classical multiple-scattering approach (Weaver, 1990) to 2-D in-plane geometry, the models of random media used in the numerical simulations may be translated to equivalent diffusivities. The theory is valid up to second order in material heterogeneity and requires the knowledge of a minimal set of statistical descriptors of the random medium which are discussed below:

1. Root Means Square (RMS) velocity fluctuations. Based on the uniform distributions of the P and S velocities in the intervals $[1, 2]$ km/s, $[2, 4]$ km/s, we deduce that these two parameters share the same RMS fractional fluctuations $\epsilon \approx 20\%$.
2. Correlation length of the fluctuations l_c. This quantity measures the typical distance beyond which any two points of the medium are statistically independent. Since the values of velocities at neighbouring grid points are uncorrelated random variables, we deduce that the correlation length l_c must be smaller than the typical grid spacing of 0.5 km and most likely of the order of 0.25 km. Because this parameter is crucial and not perfectly known, we scan a wide range of values in our computations.
3. Spatial correlation function of the fluctuations $C(r)$ (r is the distance between any two points in the medium). Finally, we must define the mathematical form of the correlation function. Here, we adopt the classical exponential $C(r) = \exp(-r/l_c)$,

which is known to be physically realizable for a wide class of heterogeneous media, in sharp contrast with the Gaussian case (S. Torquato, 2002).

In addition to the parameters listed above, we take a background velocity for P and S waves of 1.5 km/s and 3 km/s, respectively, and a central frequency of 2 Hz.

The results of the calculations are show in Figure 15a where we plot the diffusivity of the regolith inferred from the numerical simulations as a function of the correlation distance. Since the diffusivity computation is perturbative and limited to sufficiently low frequencies (or equivalently low correlation distances), we use a classical diagnostic of failure of perturbation theory which stipulates that the mean free path of S waves cannot be smaller than the correlation length (Calvet & Margerin, 2012). Examination of Figure 15b), which displays the scattering mean free path of S waves as a function of the correlation distance, reveals that our calculations should be valid except for the largest values of the correlation distance ($l_c \geq 0.48\,\mathrm{km}$).

The diffusivity varies over several orders of magnitude from $l_c = 0.02\,\mathrm{km}$ to $l_c \approx 0.1$ and becomes weakly dependent of the correlation distance for $l_c > 0.1\,\mathrm{km}$ with typical values of the order of $0.5 - 0.7\,\mathrm{km}^2/\mathrm{s}$. This range of diffusivities is typical of the upper part of the crust on the Moon (Dainty et al., 1974). Note that because the diffusivity is essentially a function of $k_s l_c$ (with k_s the S wavenumber), increasing the correlation length is equivalent to increasing the central frequency of the waves. Hence, the model predicts a weak frequency dependence of the diffusivity which agrees with the observed weak frequency dependence of the envelope shapes of HF events. The diffusivity found in the numerical simulations is somewhat lower than the one proposed by Lognonné et al. (2020) of the order of $80\,\mathrm{km}^2/\mathrm{s}$. This may not come as a surprise for at least two reasons: (1) The S wave velocity of the regolith adopted in the present study is a factor of 2 lower than in (Lognonné et al., 2020). Such a velocity drop entails a reduction of the diffusivity by a factor 4 because the arrival time of the maximum energy of diffuse waves scales like R^2/D (with R the hypocentral distance) (2) The second obvious reason, but difficult to quantify, is the different assumption on the vertical distribution of heterogeneity between Lognonné et al. (2020) (vertically uniform) and the present study (strongly stratified). Hence the value given in Lognonné et al. (2020) can be understood as an average between a strongly scattering regolith and a transparent lower crust. As observed on the Moon (Gillet et al., 2017), vertical stratification of heterogeneity is highly probable and will be an important topic for future investigations of the crustal structure of Mars.

4 Conclusions and Outlook

The signals of the three event types that comprise the high frequency family (i.e. VF, HF and 2.4 Hz) are consistent with a seismic source within the crust and the envelope shapes can be explained by seismic wave propagation effects in a strongly stratified medium with low attenuation in the crust and a shallow layer with strong scattering. While the strongly scattered signal shows some resemblance to moonquakes, the shorter coda duration and the existence of two distinct phases makes Mars appear as intermediate between Earth and the Moon in terms of seismic scattering and attenuation. Analysis of marsquakes thus requires a hybrid approach that combines lunar and terrestrial methods; unlike the Moon traditional travel time location algorithms can be readily applied, but successful analyses cannot rely on travel time picks in the time domain alone, and energy envelope approaches are required to obtain source mechanisms, event locations, and event magnitudes.

The bulk of the HF events is located in a similar distance range as the major LF events (Giardini et al., 2020) in the catalogue, but this may be purely coincidental due to our choice of crustal velocities. With independent constraints on the velocities, e.g.

through receiver function analysis (Lognonné et al., 2020) or observation of surface waves, the distance uncertainties can be reduced and the distance of the high frequency events may potentially be correlated with surface features, even in the absence of azimuth estimates, and interpreted in a seismo-tectonic context. Distance clustering of the events likely implies that the events cluster in one location and azimuth as seen from the lander, as the opposite assumption would suggest that InSight has landed by chance in the center of a circular distribution of events.

Moreover, as the envelope shapes are sensitive to the subsurface structure they may be used to further constrain it, but due to the strong trade-offs demonstrated here, independent constraints are needed. We find the suggestion of a 10 km thick layer by Lognonné et al. (2020) based on receiver functions compatible with the generation of the guided phases discussed here. A robust conclusion can be drawn on seismic attenuation, independent of the detailed velocity structure: as high-frequency seismic waves propagate over significant time and distance, high Q structure needs to be present. Here we interpret the crust to have low attenuation and show that the signals observed can be explained by such a wave propagation model. It remains difficult, however, to exclude for example a more local and shallower propagation channel. Importantly, additional arrivals would be expected if the high-Q propagation channel (i.e. the crust) would feature strong internal discontinuities and the absence of such phases suggests that such discontinuities are either not present or not very strong. As also argued by Lognonné et al. (2020), the Q values we find here are compatible with the presence of small amounts of volatiles in the crust but incompatible with the presence of liquid water.

It is also apparent, that the MQS distance estimation procedures should be extended by using a distribution of crustal velocities rather than a single model to account for the uncertainty in crustal velocities. The simple linear move-out assumption for computing traveltimes of the guided phases is likely accurate enough given the uncertainty on the crustal models. It allows us to use very few crustal parameters (i.e. P and S velocity) rather than a complete 1D model and in this way simplifies the probabilistic location approach (Böse et al., 2017) significantly.

Two important questions will need to be addressed in future work: firstly, the exact mechanism of the 2.4 Hz resonance with its high vertical-to-horizontal ratio and the absence of overtones remains poorly understood at this point. Secondly, the very large horizontal amplitudes of the VF events, partly even increasing with frequency, cannot be explained with the propagation model described in this paper and needs to be addressed separately.

Acknowledgments

The authors thank the editor Deanne Rogers, two anonymous reviewers, and Francis Nimmo for helpful comments on the manuscript.

The InSight seismic event catalogue version 3 and waveform data are available from the IPGP Datacenter and IRIS-DMC (InSight Mars SEIS Data Service, 2019; InSight Marsquake Service, 2020), as are previous catalogue versions. Seismic waveforms are also available from NASA PDS (National Aeronautics and Space Administration Planetary Data System, `https://pds-geosciences.wustl.edu/missions/insight/seis.htm`). All data and code to reproduce the figures are available online (van Driel, 2021).

We acknowledge NASA, CNES, their partner agencies and Institutions (UKSA, SSO, DLR, JPL, IPGP-CNRS, ETHZ, IC, MPS-MPG) and the flight operations team at JPL, SISMOC, MSDS, IRIS-DMC and PDS for providing SEED SEIS data.

AK, DG, JC, and SCS acknowledge support from ETHZ through the ETH+ funding scheme (ETH+02 19-1:“Planet Mars”). This work was supported by grants from the Swiss National Supercomputing Centre (CSCS) under project ID s922, and the European Research Council (ERC) under the EU's Horizon 2020 programme (grant No. 714069). L.M. acknowledges the financial support from CNES (Insight Participating Scientist Grant) and ANR MAGIS-19-CE31-0008-05.

Visualizations were created with Matplotlib (Hunter, 2007), data was processed with NumPy (Oliphant, 2006), Scipy (Jones et al., 2001), ObsPy (Krischer et al., 2015) and custom software developed by gempa GmbH. The numerical wave propagation simulations are based on the Salvus software suite (`mondaic.com`, Afanasiev et al., 2019).

This is InSight Contribution Number 178.

References

Afanasiev, M., Boehm, C., van Driel, M., Krischer, L., Rietmann, M., May, D. A., … Fichtner, A. (2019). Modular and flexible spectral-element waveform modeling in two and three dimensions. *Geophys. J. Int.*, *216*, 1675–1692. doi: 10.1093/gji/ggy469

Akkermans, E., & Montambaux, G. (2007). *Mesoscopic physics of electrons and photons.* Cambridge university press.

Banerdt, W. B., Smrekar, S. E., Banfield, D., Giardini, D., Golombek, M., Johnson, C. L., … Wieczorek, M. A. (2020). Initial results from the InSight mission on Mars. *Nat. Geosci.*, *13*(3), 183–189. doi: 10.1038/s41561-020-0544-y

Banerdt, W. B., Smrekar, S. E., Lognonné, P. H., Spohn, T., Asmar, S., Banfield, D., … Hurst, K. (2013). InSight: A Discovery Mission to Explore the Interior of Mars. In *44th lunar planet. sci. conf.* (p. 1915).

Banfield, D. J., Spiga, A., Newman, C., Forget, F., Lemmon, M. T., Lorenz, R. D., … Banerdt, W. B. (2020). The Atmosphere of Mars as Observed by InSight. *Nat. Geosci.*. doi: 10.1038/s41561-020-0534-0

Besserer, J., Nimmo, F., Wieczorek, M. A., Weber, R. C., Kiefer, W. S., McGovern, P. J., … Zuber, M. T. (2014). GRAIL gravity constraints on the vertical and lateral density structure of the lunar crust. *Geophys. Res. Lett.*, *41*(16), 5771–5777. doi: 10.1002/2014GL060240

Birch, F. (1961). The velocity of compressional waves in rocks to 10 kilobars: 2. *J. Geophys. Res.*, *66*(7), 2199–2224. doi: 10.1029/JZ066i007p02199

Blanchette-Guertin, J.-F., Johnson, C., & Lawrence, J. F. (2012, jun). Investigation of scattering in lunar seismic coda. *J. Geophys. Res.*, *117*(E6), E06003. Retrieved from `http://doi.wiley.com/10.1029/2011JE004042` doi: 10.1029/2011JE004042

Böse, M., Clinton, J. F., Ceylan, S., Euchner, F., van Driel, M., Khan, A., … Banerdt, W. B. (2017). A probabilistic framework for single-station location of seismicity on Earth and Mars. *Phys. Earth Planet. Inter.*, *262*, 48–65. doi: 10.1016/j.pepi.2016.11.003

Böse, M., Giardini, D., Stähler, S. C., Ceylan, S., Clinton, J. F., van Driel, M., … Banerdt, W. B. (2018). Magnitude Scales for Marsquakes. *Bull. Seismol. Soc. Am.*, *108*(5A), 2764–2777. doi: 10.1785/0120180037

Calvet, M., & Margerin, L. (2012). Velocity and attenuation of scalar and elastic waves in random media: A spectral function approach. *The Journal of the Acoustical Society of America*, *131*(3), 1843–1862.

Ceylan, S., Clinton, J. F., Giardini, D., Böse, M., Charalambous, C., van Driel, M., … Perrin, C. (2020). Companion guide to the Marsquake catalog from InSight, sols 0–478: Data content and non-seismic events. *Phys. Earth Planet. Inter.*, *309*(August), 106597. doi: 10.1016/j.pepi.2020.106597

Clinton, J. F., Ceylan, S., van Driel, M., Giardini, D., Stähler, S. C., Böse, M., … Stott, A. E. (2020). The Marsquake catalogue from InSight, sols 0–478. *Phys. Earth Planet. Inter.*, 106595. doi: 10.1016/j.pepi.2020.106595

Clinton, J. F., Giardini, D., Böse, M., Ceylan, S., van Driel, M., Euchner, F., … Teanby, N. A. (2018). The Marsquake Service: Securing Daily Analysis of SEIS Data and Building the Martian Seismicity Catalogue for InSight. *Space Sci. Rev.*, *214*(8), 133. doi: 10.1007/s11214-018-0567-5

Dahmen, N. L., Clinton, J. F., Ceylan, S., van Driel, M., Giardini, D., Khan, A., … Banerdt, W. B. (2020). Super high frequency events: a new class of events recorded by the InSight seismometers on Mars. *J. Geophys. Res. Planets.* doi: 10.1029/2020je006599

Dainty, A. M., & Toksöz, M. (1981). Seismic codas on the Earth and the Moon: a comparison. *Phys. Earth Planet. Inter.*, *26*(4), 250–260. doi: 10.1016/0031-9201(81)90029-7

Dainty, A. M., Toksöz, M. N., Anderson, K. R., Pines, P. J., Nakamura, Y., & Latham, G. (1974). Seismic scattering and shallow structure of the moon in oceanus procellarum. *The Moon*, *9*(1-2), 11–29.

Giardini, D., Lognonné, P. H., Banerdt, W. B., Pike, W. T., Christensen, U., Ceylan, S., … Yana, C. (2020). The seismicity of Mars. *Nat. Geosci.*, *13*(3), 205–212. doi: 10.1038/s41561-020-0539-8

Gillet, K., Margerin, L., Calvet, M., & Monnereau, M. (2017). Scattering attenuation profile of the moon: Implications for shallow moonquakes and the structure of the megaregolith. *Physics of the Earth and Planetary Interiors*, *262*, 28–40.

Gyalay, S., Nimmo, F., Plesa, A. C., & Wieczorek, M. (2020). Constraints on Thermal History of Mars From Depth of Pore Closure Below InSight. *Geophys. Res. Lett.*, *47*(16). doi: 10.1029/2020GL088653

Hunter, J. D. (2007). Matplotlib: A 2D graphics environment. *Comput. Sci. Eng.*, *9*(3), 90–95.

InSight Mars SEIS Data Service. (2019). *Seis raw data, insight mission.* IPGP, JPL, CNES, ETHZ, ICL, MPS, ISAE-Supaero, LPG, MFSC. Retrieved from `http://datacenter.ipgp.fr/networks/detail/XB_2016/` doi: 10.18715/SEIS.INSIGHT.XB_2016

InSight Marsquake Service. (2020). *Mars seismic catalogue, insight mission; v3 2020-07-01.* ETHZ, IPGP, JPL, ICL, ISAE-Supaero, MPS, Univ. Bristol. Retrieved from `http://www.insight.ethz.ch/seismicity/catalog/v3` doi: 10.12686/a8

Johnson, C. L., Mittelholz, A., Langlais, B., Russell, C. T., Ansan, V., Banfield, D., … Banerdt, W. B. (2020). Crustal and time-varying magnetic fields at the InSight landing site on Mars. *Nat. Geosci.*. doi: 10.1038/s41561-020-0537-x

Jones, E., Oliphant, T., Peterson, P., & Others. (2001). *SciPy: Open source scientific tools for Python.* (http://www.scipy.org/)

Kennett, B. L. (1989). On the nature of regional seismic phases-I. Phase representations for Pn, Pg, Sn, Lg. *Geophys. J. Int.*, *98*(3), 447–456. doi: 10.1111/j.1365-246X.1989.tb02281.x

Knapmeyer, M., & et al. (2021). Marsquake activity driven by the sun? *submitted to LPSC 2021.*

Krischer, L., Megies, T., Barsch, R., Beyreuther, M., Lecocq, T., Caudron, C., & Wassermann, J. (2015). ObsPy: a bridge for seismology into the scientific Python ecosystem. *Comput. Sci. Discov.*, *8*(1), 014003. doi: 10.1088/1749-4699/8/1/014003

Latham, G. V., Ewing, M., Press, F., Sutton, G., Dorman, J., Nakamura, Y., … Duennebier, F. (1970). Passive Seismic Experiment. *Science*, *167*(3918), 455–457.

Lognonné, P. H., Banerdt, W. B., Giardini, D., Pike, W. T., Christensen, U., Laudet, P., … Wookey, J. (2019). SEIS: Insight's Seismic Experiment for Internal Structure of Mars. *Space Sci. Rev.*, *215*(1), 12. doi: 10.1007/s11214-018-0574-6

Lognonné, P. H., Banerdt, W. B., Pike, W. T., Giardini, D., Christensen, U., Garcia, R. F., … Zweifel, P. (2020). Constraints on the shallow elastic and anelastic structure of Mars from InSight seismic data. *Nat. Geosci.*, *13*(3), 213–220. doi: 10.1038/s41561-020-0536-y

Nakamura, Y., Lammlein, D., Latham, G. V., Ewing, M., Dorman, J., Press, F., & Toksöz, N. (1973). New seismic data on the state of the deep lunar interior. *Science*, *181*(4094), 49–51. doi: 10.1126/science.181.4094.49

Nolet, G. (2009). Slabs do not go gently. *Science*.

Oliphant, T. E. (2006). *Guide to NumPy*. http://www.trelgol.com.

Ryzhik, L., Papanicolaou, G., & Keller, J. B. (1996). Transport equations for elastic and other waves in random media. *Wave motion*, *24*(4), 327–370.

S. Torquato. (2002). *Random heterogeneous materials: Microstructure and macroscopic properties*. Berlin: Springer-Verlag.

Scholz, J. R., Widmer-Schnidrig, R., Davis, P., Lognonné, P., Pinot, B., Garcia, R. F., … Banerdt, W. B. (2020). Detection, Analysis, and Removal of Glitches From InSight's Seismic Data From Mars. *Earth Sp. Sci.*, *7*(11), 1–25. doi: 10.1029/2020EA001317

Siegfried, R. W., McQueen, R. G., & Simmons, G. (1981). Shock-induced microfractures in six terrestrial igneous rocks characterized with differential strain analysis. *J. Geophys. Res. Solid Earth*, *86*(B7), 6205–6218. doi: 10.1029/JB086iB07p06205

Storchak, D. a., Schweitzer, J., & Bormann, P. (2003). The IASPEI Standard Seismic Phase List. *Seismol. Res. Lett.*, *74*(6), 761–772. doi: 10.1785/gssrl.74.6.761

van Driel, M. (2021). *Data and Software Data from the article 'High frequency seismic events on Mars observed by InSight'.* doi: 10.5281/zenodo.4383084

Weaver, R. L. (1990). Diffusivity of ultrasound in polycrystals. *Journal of the Mechanics and Physics of Solids*, *38*(1), 55–86.

Wieczorek, M. A., Neumann, G. A., Nimmo, F., Kiefer, W. S., Taylor, G. J., Melosh, H. J., … Zuber, M. T. (2013). The Crust of the Moon as Seen by GRAIL. *Science*, *339*(6120), 671–675. doi: 10.1126/science.1231530